Magnetic-Field Amplification in the Thin X-ray Rims of SN1006

Sean M. Ressler[1], Satoru Katsuda[2], Stephen P. Reynolds[3], Knox S. Long[4], Robert Petre[5], Brian J. Williams[5], & P. Frank Winkler[6]

[1] Department of Physics, University of California Berkeley, Berkeley, CA 94720, USA

[2]Institute of Space and Astronautical Science (ISAS), Japan Aerospace Exploration Agency (JAXA), 3-1-1 Yoshinodai, Chuo, Sagamihara, Kanagawa 252-5210, Japan

[3]Physics Department, North Carolina State University, Raleigh, NC 27695, USA

[4]Space Telescope Science Institute, 3700 San Martin Drive, Baltimore, MD 21218, USA

[5]NASA Goddard Space Flight Center, Greenbelt, MD 20771, USA

[6]Department of Physics, Middlebury College, Middlebury, VT 05753, USA

Received ____________________; accepted ____________________

ABSTRACT

Several young supernova remnants (SNRs), including SN1006, emit synchrotron X-rays in narrow filaments, hereafter thin rims, along their periphery. The widths of these rims imply 50 to 100μG fields in the region immediately behind the shock, far larger than expected for the interstellar medium compressed by unmodified shocks, assuming electron radiative losses limit rim widths. However, magnetic-field damping could also produce thin rims. Here we review the literature on rim width calculations, summarizing the case for magnetic-field amplification. We extend these calculations to include an arbitrary power-law dependence of the diffusion coefficient on energy, $D \propto E^{\mu}$. Loss-limited rim widths should shrink with increasing photon energy, while magnetic-damping models predict widths almost independent of photon energy. We use these results to analyze Chandra observations of SN 1006, in particular the southwest limb. We parameterize the full widths at half maximum (FWHM) in terms of energy as FWHM $\propto E_{\gamma}^{m_E}$. Filament widths in SN1006 decrease with energy; $m_E \sim -0.3$ to -0.8, implying magnetic field amplification by factors of 10 to 50, above the factor of 4 expected in strong unmodified shocks. For SN 1006, the rapid shrinkage rules out magnetic damping models. It also favors short mean free paths (small diffusion coefficients) and strong dependence of D on energy ($\mu \geq 1$).

Subject headings: acceleration of particles – ISM: individual objects (SN 1006) – ISM: magnetic fields – ISM: supernova remnants – X-rays: ISM

1. Introduction

Cosmic synchrotron sources, such as jets in active galactic nuclei, radio halos and relics in clusters of galaxies, pulsar-wind nebulae, and shell supernova remnants (SNRs), demonstrate the ubiquity of power-law distributions of relativistic electrons. Understanding the origins of these fast particles is necessary to learn about these objects' energy budgets and evolution. The synchrotron flux density emitted by a source depends roughly on the product of the energy density of relativistic electrons u_e and the magnetic field u_B, but an independent determination of magnetic-field strengths in synchrotron sources has proven elusive. The minimum energy of a synchrotron source occurs when the two energy densities are roughly equal ("equipartition;" actually, $u_e = (4/3)u_B$; e.g., Pacholczyk 1970). However, it is not clear whether the unseen population of relativistic protons should also be included, and if so, what the proton-to-electron energy ratio should be. Furthermore, there is no obvious physical reason to expect equipartition. The argument for equipartition derives from attempts to explain extragalactic radio sources in which the total energy budget is so large that it was of interest to find a lower bound (Burbidge 1956). However, many other synchrotron sources, including SNRs, release a relatively small fraction of their total energy content as synchrotron emission, so could easily afford to be far from equipartition (in either direction).

Although magnetic fields are not dynamically important in SNRs (e.g., Jun & Jones 1999), their strength is critical in determining the maximum energy to which particles can be accelerated. For the diffusive shock acceleration process (DSA; e.g., Blandford & Eichler 1987), the time $\tau(E)$ to accelerate particles to energy E depends on the diffusion coefficient D and the shock velocity $v_{\rm shock}$ by $\tau(E) \sim D/v_{\rm shock}^2$. For relativistic particles, $D = \lambda c/3$. Then in "Bohm-like" diffusion, where the mean free path λ is assumed proportional to the particle gyroradius ($\lambda = \eta r_{\rm g} = \eta E/eB$), $\tau(E) \propto 1/B$, and higher magnetic fields result in more rapid acceleration and higher maximum energies. This is independent of which of several competing mechanisms ultimately limits acceleration (finite time since onset of acceleration, radiative losses, or escape). Note that for the above description of the diffusion coefficient, taking $\eta = 1$ is called Bohm diffusion or the "Bohm limit." It corresponds to $\lambda = r_g$, often assumed to be the shortest physically plausible mean free path. However, in a turbulent wave field, it is not clear whether this is a true limit, or even what kind of average value for the magnetic-field strength should be used to calculate r_g (e.g., Reville & Bell 2013).

Largely by exclusion of competing hypotheses, Galactic cosmic ray acceleration is now widely attributed to SNR shocks. The consensus is that SNRs can accelerate particles up to the "knee," the slight inflection and steepening around 3 PeV (3×10^{15} eV). (No plausible version of SNR-based DSA produces the maximum energies observed in cosmic rays of above 10^{19} eV [e.g., Abraham et al. 2008], for which an extragalactic origin is presumed.) However, since the work of Lagage & Cesarsky (1983), it has been clear that typical estimates of magnetic-field strengths behind SNR shocks of a few μGauss (the mean interstellar magnetic field multiplied by the shock compression ratio, r, taken to be 4 for strong nonrelativistic shocks), result in maximum energies that fall short of the "knee" by an order of magnitude or more. These estimates of B are based on measurements of the interstellar magnetic field strength within a few kpc of the Sun, which is about 2 – 3 μGauss (Lyne & Smith 1989). Simple compression in a strong shock with adiabatic index $\gamma = 5/3$ (i.e., unmodified by cosmic rays) would produce downstream values larger by a factor of up to 4 (no amplification if the shock velocity is parallel to the field, a factor of 4 increase if perpendicular). Thus magnetic fields larger than about 12 μGauss require an additional process of amplification. Independent methods of estimating interstellar magnetic-field strengths, such as Zeeman splitting in molecular lines, are not relevant to SNR environments.

Thus the plausibility of models in which SNR shocks produce Galactic cosmic rays up to the "knee" may depend on observational determinations of the post-shock magnetic field strength. Fortunately, the realization that young SNRs can produce synchrotron emission into the X-ray band has made available a new, potentially powerful method for such determinations. Several young SNRs show thin (a very small fraction of their diameter), synchrotron-emitting filaments along their edges. The widths of these rims in the radial direction have been used to infer estimates for the post-shock magnetic field strength and presented as evidence for significant magnetic field amplification by strong shocks, as we shall review in detail below. The complexity of the calculations used to infer the magnetic field magnitude varies significantly from simple analytic approximations to detailed numerical calculations, but the consensus from these studies is that field amplification well beyond a factor of four is required to explain the X-ray observations.

Thin synchrotron rims present a well-defined problem. While synchrotron emissivity may suddenly turn on at the shock front due to particle acceleration and magnetic-field compression (or amplification) there, turning it off again only about a tenth of a parsec downstream is not so simple: one must either eliminate the radiating particles or the magnetic field. Both possibilities have been suggested. Radiative energy losses as particles advect and diffuse downstream will eventually lower electron energies below the level at which synchrotron X-rays can be produced. More rapid synchrotron losses for higher electron energies then predict that rims will become thinner at higher photon energies. However, it is also possible that magnetic fields somehow decay behind the shock, with a length scale (almost) independent of electron energy, predicting rims whose thickness is relatively constant with photon energy.

In the energy-loss scenario, the rate at which rims become thinner as observing energy rises depends on electron transport. If electrons are simply advected downstream, rim widths l depend only on the magnetic-field strength, and drop quite rapidly with increasing photon energy, $l \propto (h\nu)^{-1/2}$ in the simplest approximation, as we describe below. However, diffusion allows electrons of the same energy to spread out spatially, diluting this effect somewhat and predicting slower drops in rim widths with energy. Measuring the rim widths at several different photon energies is thus key to discriminating among models.

The remnant of the Type Ia Supernova of AD 1006 is well suited for this analysis, as its large angular size coupled with *Chandra*'s high spatial resolution allows accurate measurements of radial profiles of the filaments: the remnant radius of about $15'$ corresponds to over 1800 *Chandra* ACIS pixels. Furthermore, the shock speeds in the synchrotron-dominated northeast (NE) and southwest (SW) edges are about 5000 km s^{-1}, as measured from their proper motion (Katsuda et al. 2009, Winkler et al. 2014), and the SNR has been detected as a TeV source (Acero et al. 2010), suggesting that SN1006 produces very high-energy cosmic rays.

Our purpose here is to consider theories of particle diffusion and magnetic-field amplification in the light of new deep observations of SN1006 made with *Chandra*. In Section 2 (summarized in Table 1), we review earlier work on filament calculations and the evidence for field amplification to establish a firm background for the new work presented here. In Section 3, we generalize previous work by allowing different energy dependence of the diffusion coefficient from Bohm-like, including Kolmogorov and Kraichnan-type diffusion, among others. We first neglect any cut-off in the electron spectrum and calculate model profiles and their energy dependence for the loss-limited (Section 3.1) and magnetically damped (Section 3.2) scenarios. We then add the effects of an electron cut-off energy (Section 3.3), and examine the effects of making the δ-function approximation for the emissivity (Section 3.4). In Section 4, we describe measurements of the widths of the nonthermal filaments in SN1006, including for the first time the SW region, making use of new high-resolution *Chandra* measurements. We find that rim widths decrease with increasing photon energy, quite rapidly in some cases. In Section 5, we use these measurements to constrain both the post-shock magnetic field and diffusion coefficient. The general narrowing of rims eliminates the magnetic-damping model for rim widths; quantitatively, we find values of post-shock magnetic field of 70 – 200 μG, comparable to those obtained in earlier work. However, the rapidity of rim shrinkage suggests that diffusion mean free paths in some areas are quite small, perhaps less than the gyroradius. We discuss these results in Section 6, including reviewing theoretical and observational work on sub-Bohm diffusion and implications for particle acceleration to high energies. We summarize our conclusions in Section 7. Finally, in the appendix, we offer a list of the results of our experience in applying the various rim models to observations, as a guide for potential future investigations.

2. Previous Work

Prior work bifurcates into two eras, an earlier one in which it was assumed that the only influence on filament shapes was synchrotron losses, followed by one beginning in 2005 when additional effects such as magnetic field damping began to be introduced. We consider first the former case; decay of magnetic field is considered in Section 2.2.

2.1. Loss-limited models

Before 2005, it was universally assumed that the shapes of nonthermal X-ray filaments observed in SNRs were due to synchrotron losses by high energy electrons (see the many references described below and in Table 1). The idea was that an electron could only travel a certain distance before losing enough energy that its radiation dropped below the X-ray band. This distance is determined by two competing transport mechanisms: advection (bulk motion of plasma) and diffusion (random motion of electrons on the scale of gyroradii). Considered separately, one can obtain simple expressions for the appropriate length scale for each in terms of the diffusion coefficient, D, the downstream plasma speed in the shock frame, $v_{\rm d}$, and the synchrotron cooling time, $\tau_{\rm synch}$. We can estimate $\tau_{\rm synch} = 1/(bB^2E)$, where $b = 1.57 \times 10^{-3}$ in cgs, from the relation $\dot{E} \propto E^2$. Thus, for $v_{\rm d} = v_{\rm shock}/4$, given by the Rankine-Hugoniot conditions for a strong adiabatic shock, we have an advective length of $l_{\rm ad} \approx v_{\rm d}\tau_{\rm synch} = (v_{\rm d})/(bB^2E)$. For a diffusion coefficient that is taken as a constant multiple, η, of the Bohm value $D = \eta C_{\rm d}E/B$, where $C_{\rm d} \equiv c/(3e)$, we arrive at a diffusive length of $l_{\rm diff} \approx \sqrt{D\tau_{\rm synch}} = \sqrt{D/(bB^2E)}$. For the values of the constants b, $C_{\rm d}$, $c_{\rm m}$, and c_1 used here and throughout, see Table 8. Now, an electron of energy E in a magnetic field radiates primarily at the frequency $\nu_m = c_{\rm m}E^2B$ so that the advection and diffusion lengths as a function of frequency are

$$l_{\rm ad} = \frac{v_d\sqrt{c_m}}{b}B^{-3/2}\nu_m^{-1/2} \tag{1}$$

and

$$l_{\rm diff} = \sqrt{\frac{\eta C_{\rm d}}{b}}B^{-3/2}. \tag{2}$$

The approximation that the electron radiates all its energy at ν_m is called the delta-function approximation. **The important result here is that $l_{\rm ad}$ varies as $\nu^{-1/2}$ while $l_{\rm diff}$ is independent of frequency.** Thus above some critical energy, E_c, and an associated photon frequency, ν_c, electrons will be able to diffuse further in a loss time than they could advect, and electron diffusion will become the dominant method of transport. $E_{\rm c}$ is found simply by equating the expressions for $l_{\rm ad}$ and $l_{\rm diff}$:

$$E_{\rm c} = \frac{v_{\rm d}}{\sqrt{\eta C_{\rm d} bB}} \approx 69.12 \text{ ergs} \left(\frac{v_{\rm d}}{1250 \text{ km s}^{-1}}\right)\left(\frac{B}{100\ \mu\text{G}}\right)^{-1/2}\eta^{-1/2} \tag{3}$$

$$h\nu_{\rm c} = \frac{c_m v_{\rm d}^2}{\eta C_{\rm d} b} \approx 3.61 \text{ keV}\left(\frac{v_{\rm d}}{1250 \text{ km s}^{-1}}\right)^2 \frac{1}{\eta}. \tag{4}$$

(We have taken $v_d = v_{\rm shock}/4 = 1250$ km s^{-1}, assuming no shock modification by cosmic rays.) Near this photon energy, both advection and diffusion are important. This simple approach was taken by Ballet (2006), Bamba et al. (2005), and Yamazaki et al. (2004) to infer magnetic field strengths of 14–87 μG in SN 1006. Vink & Laming (2003) used a similar technique for Cas A, and estimated B to be ~ 100 μG.

Parizot et al. (2006) adopted a somewhat more sophisticated approach, combining both processes in the steady state form of the one-dimensional transport equation to solve for the post-shock electron distribution $f(p, x)$ (Völk et al. 1981):

$$v\frac{\partial f}{\partial x} - D\frac{\partial^2 f}{\partial x^2} + \frac{f}{\tau_{\rm synch}} = 0, \tag{5}$$

where the loss term $f/(\tau_{\rm synch})$ assumes that an electron maintains constant energy as it travels away from the injection site until a catastrophic dump at time $\tau_{\rm synch}$. Here the shock is at $x = 0$ and $x > 0$ is the distance downstream. The solution to this equation is $f(p, x) \propto e^{-|x|/a}$, with the scale length a given by:

$$a = \frac{2D/v_{\rm d}}{\sqrt{1 + \frac{4D}{v_{\rm d}^2 \tau_{\rm synch}}} - 1} \tag{6}$$

(Berezkho & Völk 2004, Parizot et al. 2006). More explicitly, in terms of electron energy E the scale length is

$$a = \frac{2\eta C_{\rm d} E/B v_{\rm d}}{\sqrt{1 + \frac{4b\eta C_{\rm d} E^2 B}{v_{\rm d}^2}} - 1}. \tag{7}$$

At a given observation frequency ν, E will depend on the magnetic field B, by $E = \sqrt{\nu/(c_m B)}$, so

$$a = \frac{2\eta C_{\rm d} c_m^{-1/2} \nu^{1/2} B^{-3/2}/v_{\rm d}}{\sqrt{1 + \frac{4b\eta C_{\rm d}\nu}{c_m v_{\rm d}^2}} - 1}. \tag{8}$$

In order to estimate the strength of the magnetic field, we invert this expression so that it is a function of observables:

$$B = \left(\frac{a c_m^{1/2} v_{\rm d} \left(\sqrt{1 + \frac{4b\eta C_{\rm d}\nu}{c_m v_{\rm d}^2}} - 1 \right)}{2\eta C_{\rm d} \nu^{1/2}} \right)^{-2/3} . \tag{9}$$

In this equation a is the scale length of the electron distribution, whereas we observe the scale length of the emitted synchrotron intensity, including line-of-sight projection effects. In the δ-function approximation of the synchrotron emissivity, $j_\nu \propto \sqrt{\nu B} f(E, x)$ ($E = pc$ for relativistic electrons), and the radial intensity for a spherical shock is

$$I_\nu(r) = 2 \int_0^{\sqrt{r_s^2 - r^2}} j_\nu \left(r_s - \sqrt{s^2 + r^2} \right) ds. \tag{10}$$

Here r is the sky-plane radius (r_s the shock radius), and s is the line-of-sight coordinate. The resulting profile will have a FWHM $= \beta a$, β a projection factor. Ballet (2006) showed that in the case of a purely exponential (in space) electron distribution and for a spherical source, the result of this integral will give $\beta = 4.6$, that is, a filament with a Full Width at Half Maximum (FWHM) of $4.6a$. Thus in terms of the observed filament width, $w_{\rm obs}$, we have

$$B = \left(\frac{w_{obs} c_m^{1/2} v_{\rm d} \left(\sqrt{1 + \frac{4b\eta C_{\rm d}\nu}{c_m v_{\rm d}^2}} - 1 \right)}{2\beta\eta C_{\rm d} \nu^{1/2}} \right)^{-2/3} . \tag{11}$$

Using this result, the post-shock magnetic field strength in the NE rim of SN1006 was estimated to be around 91-110 μG for $w_{obs} = 20''$, an amplification of roughly 30-37 for an ambient 3 μG field (Parizot et al. 2006). While those authors did not make use of the fact, we note that the inferred value of B depends on observing frequency.

It should be noted that the projection factor $\beta = 4.6$ is entirely dependent on the exponential form of the synchrotron emissivity given from the solution of (5), which may not be valid, as well as on the assumption of exact sphericity. This is an important caveat, as the width of the rims scales as $B^{-3/2}$ (from equation (8)), so, since the width is inversely proportional to the projection factor, β, the above estimates for the post-shock magnetic field strength are proportional to $\beta^{2/3}$. In our later calculations, however, we do not assume a simple constant projection factor and perform the full numerical line-of-sight integration.

Finally, the most sophisticated synchrotron-loss based models of Berezhko et al. (2003), Berezhko & Völk (2004), Cassam-Chenaï et al. (2007), Morlino et al. (2010) and Rettig & Pohl (2012) use an electron distribution obtained by solving the continuous energy loss convection-diffusion equation (properly, the advection-diffusion equation):

$$v\frac{\partial f}{\partial x} - \frac{\partial}{\partial x}\left(D\frac{\partial f}{\partial x}\right) - \frac{\partial}{\partial E}\left(bB^2E^2f\right) = K_0 E^{-s} e^{-E/E_{\rm cut}} \delta(x), \tag{12}$$

where it is assumed that electrons are injected at the shock and follow a power-law energy distribution with an exponential cut-off: ($N(E) \propto E^{-s} e^{E/E_{\rm cut}}$, where $s = 2.2$ – the value appropriate for SN 1006). The electron distribution obtained from solving this equation is convolved with the single-particle emissivity and then integrated along lines of sight (see equation 10) to compute radial intensity profiles. The magnetic-field strength for SN 1006 predicted using this method is in the range of 90-130 μG, an amplification of roughly 30–43 for an ambient field of 3 μG (Berezhko et al. 2003, Morlino et al. 2010, Rettig & Pohl 2012).

2.2. Energy Dependence of the Filament Widths

In almost all previous calculations, the energy dependence of the filament width was ignored and profiles were fit at a single photon energy. One exception to this is the work of Araya et al. (2010) in their analysis of the shapes of the rims of Cas A. Interestingly, while Araya et al. found no significant energy dependence in the rim widths between the energy ranges 3–6 keV and 6–10 keV, they did report a small but non-negligible difference between widths at 0.3–2 and 3–6 keV. However, they did not use this result as a parameter constraint. Here we show that this dependence has important physical consequences for

Table 1: Previous Magnetic Field Strength Estimates for SN1006

Note: $B_0 \equiv B$ directly behind the shock

Paper	Technique	SN1006 B_0 estimate	Amplification Factor (For ISM Field of 3 μG)
Araya et al. (2010)	Catastrophic Dump C-D equation	-	-
Ballet (2005)	Equated $l_{\rm diff}$ to rim sizes	87 μ G	29
Bamba et al. (2005)	Equated $\max(l_{\rm diff}, l_{\rm ad})$ to rim sizes	-	-
Berezhko et al. (2003)	Time dependent continuous loss C-D equation	$\sim 100\mu$G	33
Berezhko & Völk (2004)	Time dependent continuous loss C-D equation	-	-
Cassam Chenaï et al. (2007)	CR modified numerical solution to C-D equation	-	-
Morlino et al. (2010)	Nonlinear DSA Model Fit	90 μG	30
Parizot et al. (2006)	Catastrophic Dump C-D equation + δ-function	91-110 μG	30-37
Rettig & Pohl (2012)	Continuous loss C-D equation	130 μG (loss limited)	43
		$\sim$65 μG (B-limited)	22
Vink & Laming (2003)	Equated $\max(l_{\rm diff}, l_{\rm ad})$ to rim sizes	-	-
Yamazaki et al. (2004)	Equated $\max(l_{\rm diff}, l_{\rm ad})$ to rim sizes	14-85 μG	5-28

parameter estimation.

In all the models we shall consider, the diffusion coefficient rises with energy. This means that electrons with lower energies will stay closer to their original fluid element while those with higher energies move about more freely. Specifically, as can be seen from Equation 6, for $\nu \gg \nu_{\rm c}$, $a \approx l_{\rm diff}$, while for $\nu \ll \nu_{\rm c}$, $a \approx l_{\rm ad}$. This behavior shows up in how the width, a, varies with energy, which we can parameterize as $a \propto E_\gamma^{m_{\rm E}}$ for a photon energy of $E_\gamma \equiv hv$. Written in this way, we have

$$m_E = -\frac{1}{2}\left(1 - \frac{4D/(v_{\rm d}^2\tau)}{1 + 4D/(v_{\rm d}^2\tau) - \sqrt{1 + 4D/(v_{\rm d}^2\tau)}}\right), \tag{13}$$

where $4D/(v_{\rm d}^2\tau) \propto E^2 B \propto \nu$, with the last proportion coming from the δ-function approximation, meaning that m_E is independent of magnetic field strength. It is also clear from equation (13) that $m_{\rm E}$ will go from $-1/2 \rightarrow 0$, or in other words that the scale length, a, will go from $a \propto E_\gamma^{-1/2} \rightarrow a \propto E_\gamma^0$, as ν goes from $0 \rightarrow \infty$ (for $D \propto E$, or in our later notation, $\mu = 1$).

2.3. Magnetic-Field Damping

In 2005 Pohl, Yan, & Lazarian introduced a more sophisticated approach, which suggested that claims of strong field amplification might be premature. They proposed several processes that could lead to an exponentially decaying magnetic field, as well as account for the narrow filamentation. In this case, rim profiles would reflect the spatial distribution of the magnetic field. Unfortunately, there are no simple predictions for the magnetic-field damping length (or detailed spatial dependence). There are a variety of physically possible damping mechanisms, so the damping length is a free parameter in models of this type (although its dependence on the immediate post-shock value of B can be preserved).

Cassam-Chenaï et al.(2007) used this idea to fit intensity profiles of the filaments in Tycho's SNR, employing a hydrodynamics code that included cosmic-ray shock modification (increased compression ratios due to energetically important particles becoming relativistic and/or escaping). They generated model profiles assuming a magnetic-field profile with exponential damping, similar to our expression in Section 3.4 below. By incorporating radio observations, they concluded that the synchrotron loss-limited model provides a slightly better fit than the magnetically damped model, though neither completely reproduces the radio profiles. More recently, Rettig and Pohl (2012) followed up by probing the observational consequences of both a magnetically damped model and a constant field model by using differences in the spectral index between the emission at the rim peak (i.e. the emission from the shock front to a FWHM distance away)and in the "plateau" (i.e. the emission from regions beyond the FWHM). Their magnetic-field estimates for both models still favor $\gtrsim 60\ \mu$G for SN1006.

Marcowith & Casse (2010) performed detailed calculations to investigate the magnetic-damping model, studying the amplification process due to linear and nonlinear cosmic-ray streaming instabilities, and identifying processes to damp the turbulent magnetic field. They report that a damping model could explain rims in the younger remnants Cassiopeia A, Tycho, and Kepler, but not in SN 1006 or G347.3–0.5 (RX J1713.7-3946). For the objects which satisfy their conditions for magnetic damping, they deduce quite high magnetic-field strengths of 200 – 300 μG.

3. Generalized Diffusion Model

Here, we will consider the case of diffusion coefficients of the form $D = \eta D_B(E_h)(E/E_h)^\mu$, where $D_B(E_h)$ is the Bohm diffusion coefficient at an arbitrary fiducial energy E_h and a magnetic field B_0, η is a constant scaling factor taken in conjunction with $D_B(E_h)$ as a free parameter, and μ parameterizes the energy dependence of D. (So for Bohm diffusion, $\eta = 1$ and $\mu = 1$.) For $\mu < 1$, E_h must be above the relevant energy range for X-ray emitting electrons, so that D remains greater than the minimum Bohm value at all energies. On the other hand, for $\mu > 1$, this energy is the lower threshold energy for this exotic type of diffusion to occur. We expect μ to be related to the power-law index n of hydromagnetic turbulence, $I(k) \propto k^{-n}$ where $I(k)$ is the wave power per unit wavenumber. Then $n = 5/3$ corresponds to a Kolmogorov spectrum, and $n = 3/2$ to a Kraichnan spectrum. In quasi-linear theory, particles have a mean free path inversely proportional to the energy density of MHD waves with wavelength comparable to the particle gyroradius, resulting in $\mu = 2 - n$ (e.g., Reynolds 2004). So Kolmogorov turbulence predicts $\mu = 1/3$ and Kraichnan, $\mu = 1/2$.

In all of the ensuing discussion we will be concerning ourselves with the consequences of these models observable in the X-ray filaments of SN1006, which we will characterize by their FWHM, $x_{1/2}$, and its energy dependence, again parametrized by m_{E}. This is explicitly written as $x_{1/2} \propto E^{m_{\mathrm{E}}}$.

For the case of $\mu = 1$ the E_h independent case, we adopt Rettig & Pohl's solution to equation (12) for the electron spatial distribution, assuming the injected spectrum to be an exponentially cut off power law with index s, integrated over $n \equiv E'/E$:

$$\begin{aligned} f(x,E) = Q_0 E^{-(s+1)} \int\limits_1^\infty \frac{n^{-s}}{\sqrt{\ln(n)}} \\ \times \exp\left[-\frac{nE}{E_{\rm cut}} - \frac{\left[l_{\rm ad}\left(1-\frac{1}{n}\right) - z(x)\right]^2}{4 l_{\rm diff}^2 \ln(n)} \right] dn, \end{aligned} \tag{14}$$

while for $\mu \neq 1$, we adopt Lerche & Schlickeiser's (1980) solution to equation (12),

$$\begin{aligned} f(x,E) = \frac{Q_0}{\sqrt{(1-\mu)}} E^{-(s+1/2+\mu/2)} \int\limits_0^1 \frac{n^{(s+\mu-2)/(1-\mu)}}{\sqrt{1-n}} \\ \times \exp\left[-\frac{n^{1/(1-\mu)}E}{E_{\rm cut}} - \frac{(1-\mu)\left[l_{\rm ad}\left(1-n^{1/(1-\mu)}\right) - z(x)\right]^2}{4 l_{\rm diff}^2 (1-n)} \right] dn, \end{aligned} \tag{15}$$

for $\mu < 1$, and

$$\begin{aligned} f(x,E) = \frac{Q_0}{\sqrt{(1-\mu)}} E^{-(s+1/2+\mu/2)} \int\limits_1^\infty \frac{n^{(s+\mu-2)/(1-\mu)}}{\sqrt{n-1}} \\ \times \exp\left[-\frac{n^{1/(1-\mu)}E}{E_{\rm cut}} - \frac{(1-\mu)\left[l_{\rm ad}\left(1-n^{1/(1-\mu)}\right) - z(x)\right]^2}{4 l_{\rm diff}^2 (1-n)} \right] dn, \end{aligned} \tag{16}$$

for $\mu > 1$. Here Q_0 is a normalization constant that does not factor into our calculations. In this formalism, all the information about the spatial dependence of the magnetic field is contained in the function $z(x)$, defined as

$$z(x) = \frac{1}{B_0^2} \int\limits_0^x B(u)^2 du. \tag{17}$$

where B_0 is the magnetic field immediately behind the shock, not the far upstream value. It is presumably amplified from its initial value to the extent demanded by the data.

Furthermore, the cut-off energy, $E_{\rm cut}$, is found by equating loss times and acceleration times, which gives, in the Bohm Limit (Rettig & Pohl 2012):

$$E_{\rm cut} = 8.3 \text{ TeV } \left(\frac{B_0}{100\mu\text{G}}\right)^{-1/2} \left(\frac{v_s}{1000 \text{ km s}^{-1}}\right). \tag{18}$$

For arbitrary diffusion coefficients, it is a straightforward generalization to show:

$$E_{\rm cut} \propto \left(\frac{B_0}{100\mu{\rm G}}\right)^{-\frac{1}{1+\mu}} \left(\frac{v_s}{1000\ {\rm km\ s^{-1}}}\right)^{\frac{2}{1+\mu}} \left(\frac{E_h}{\eta}\right)^{\frac{1}{1+\mu}}. \tag{19}$$

These analytic solutions were derived under the assumption that $B(x)^2 D(x)$ is a constant with respect to x, the distance from the shock. This condition is somewhat peculiar in that it is only naturally satisfied if B is constant, since the spatial dependence of $D(x)$ is contained in its dependence on B. For a field that evolves due to flux conservation, we expect this to be a reasonable approximation within a thin rim. On the other hand, for a rapidly varying magnetic field (e.g. one that exponentially decays in space), this imposes a rapid variation in $D(x)$ with x, which may or may not be realistic. However, we do not expect this to affect our results at the qualitative level, and some justification for this assumption can be found in Rettig & Pohl (2012).

Using this spectrum of electrons, intensity profiles are then obtained by first evaluating the synchrotron emissivity

$$j_\nu = c_3 B \int_0^\infty G(y) f(x,E) dE \tag{20}$$

with $y \equiv \nu/c_1 E^2 B$, and $G(y) \equiv y \int_y^\infty K_{5/3}(z)dz$, in a slightly different notation from Pacholczyk (1970); here $K_{5/3}(z)$ is a Bessel function of the second kind with imaginary argument. Then, integrating along lines of sight:

$$I_\nu(r) = 2 \int_0^{\sqrt{r_s^2-r^2}} j_\nu\left(r_s - \sqrt{s^2+r^2}\right) ds. \tag{21}$$

To characterize the size of the filaments, we use the FWHM of this radial intensity, denoted $x_{1/2}$. Then, we write $x_{1/2} \propto E_\gamma^{m_E}$ to characterize the energy dependence of the FWHM at each photon energy by

$$m_E = \frac{\log(x_{1/2}/x'_{1/2})}{\log(E_\gamma/E'_\gamma)}. \tag{22}$$

In a brief aside, we note that one can get qualitative results for the behavior of m_E when $\mu \neq 1$ by noting that $l_{\rm diff} = \sqrt{D\tau_{\rm synch}} \propto E^{(\mu-1)/2} \propto \nu^{(\mu-1)/4}$ in the delta function approximation. Furthermore, we can generalize equation (13) by using the new diffusion coefficient in equation (6). This gives

$$m_E = -\frac{1}{2}\left(\mu - \frac{4(\mu+1)D/(v_{\rm d}^2\tau)}{2 + 8D/(v_{\rm d}^2\tau) - 2\sqrt{1+4D/(v_{\rm d}^2\tau)}}\right). \tag{23}$$

Now at a photon energy of 2 keV, we can write $D(2\text{ keV}) = \eta_2 D_B(2keV)$, and coupled with a modified equation (9), we can solve uniquely for η_2 and the maximum field strength B_0 by measuring w_{obs} and m_E at 2 keV. The results of using this approximate result are shown in Table 2.

When performing the full numerical calculation of FWHMs, we distinguish between two parametrizations of the magnetic field, called the "loss-limited model" and the "magnetically damped model." That is, we can use the appropriate electron distribution (14), (15), or (16) for both cases, varying the spatial dependence of B to select either loss-limited or magnetically damped situations. We will initially neglect the cut-off in the injected electron spectrum in order to more clearly highlight the energy dependence of each model; we include the effects of cut-offs in Section 3.4.

3.1. Loss-Limited Model

In the loss-limited model, we assume the magnetic field is spatially uniform, a good approximation if we expect it to evolve by flux conservation in the narrow region behind the shock. Then the function $z(x)$ as defined in Equation (17) reduces to just x. With only two free parameters, the scaling factor for the diffusion coefficient at 2 keV, η_2 and the maximum field strength B_0, we can fit the observed filaments and their energy dependence uniquely for any value of μ. For the case of Bohm diffusion ($\mu = 1$), the simple estimate of

Table 2. Best fit parameters for the Filaments in varying values of μ (Analytic Results)

	Filament 1		Filament 2		Filament 3	
μ	η_2	B_0	η_2	B_0	η_2	B_0
0	7 ± 4	165 ± 21	0 ± 0.04	143 ± 52	0 ± 0.007	81 ± 3
1/3	2.4 ± 0.9	130 ± 8	0 ± 1.2	143 ± 39	0 ± 0.008	80.7 ± 0.9
1/2	1.8 ± 0.6	123 ± 7	0 ± 1.2	144 ± 35	0 ± 0.007	80.7 ± 1.2
1	1.1 ± 0.4	113 ± 4	0 ± 1.1	145 ± 26	0 ± 0.018	80.7 ± 2
1.5	$.8 \pm 0.3$	108 ± 3	0 ± 1.0	145 ± 21	0 ± 0.03	80.7 ± 1
2	$.7 \pm 0.3$	105 ± 3	$.2 \pm 0.9$	150 ± 21	$0 \pm 3 \times 10^{-7}$	80.7 ± 1.1

	Filament 4		Filament 5	
μ	η_2	B_0	η_2	B_0
0	0 ± 0.001	118 ± 1.1	$0 \pm 1.3 \times 10^5$	1000 ± 500
1/3	$0 \pm 2 \times 10^{-5}$	117.9 ± 0.8	$0 \pm 2 \times 10^4$	0 ± 60000
1/2	0 ± 0.0003	117.9 ± 1.4	0 ± 120	300 ± 300
1	0 ± 0.016	117.9 ± 0.8	5 ± 5	160 ± 40
1.5	0 ± 0.0012	117.9 ± 0.8	2.5 ± 1.7	140 ± 20
2	$0 \pm 1 \times 10^{-8}$	117.9 ± 1.5	1.7 ± 0.9	125 ± 9

*Results of fitting equation (6) to the data using a Levenberg-Marquardt least-squares algorithm. The stated uncertainties are estimated as 1σ. B_0 is in units of μG while η_2 is a dimensionless quantity representing the ratio of the fitted diffusion coefficient to the Bohm-limit diffusion coefficient at a photon energy of 2 keV.

section 1.1.1 resulted in an equation (13) for m_E which is independent of B_0. This behavior is preserved in the full calculation, and even for values of μ differing from 1 the energy dependence only weakly depends on the magnetic field strength.

3.1.1. Energy Dependence of the Loss-Limited Model

In the loss limited model, we still see the same general behavior of the FWHM with energy as the calculation of Section 1.2. There is a clear transition between energies where advection is dominant to those where diffusion is dominant, with m_E dropping from –1/2 to $(\mu - 1)/4$. A plot of this behavior for several values of μ is shown in Figure 1 and an example of calculated profiles is shown in Figure 2. A crucial point to make is that the magnitude of the diffusion coefficient is by far the most important factor in determining $m_{\rm E}$. For Bohm-type diffusion (i.e. $\mu = 1$) this mapping is 1-1, while for $\mu \neq 1$ there exists only a weak dependence of $m_{\rm E}$ on the magnitude of the post-shock magnetic field. Thus, the observation of $m_{\rm E}$ is a direct probe of the properties of the diffusion coefficient, including both its magnitude and behavior with energy, as can be clearly seen in Figure 3.

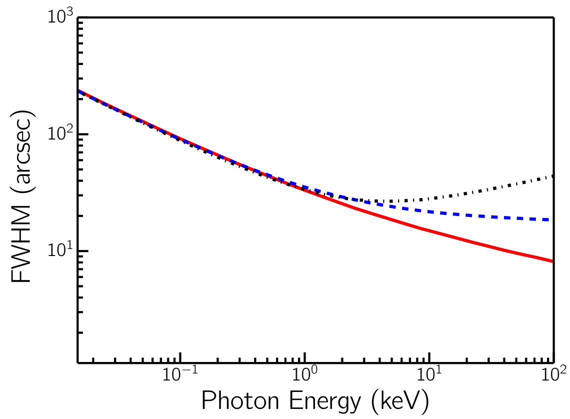

Fig. 1.— Energy dependence of filament widths for different diffusion coefficients, for pure power-law electron spectra without a cut-off. Solid line is Kolmogorov-like ($D \propto E^{1/3}$), dashed line is Bohm-like ($D \propto E$), and dot-dashed line is for $\mu = 2$ ($D \propto E^2$).

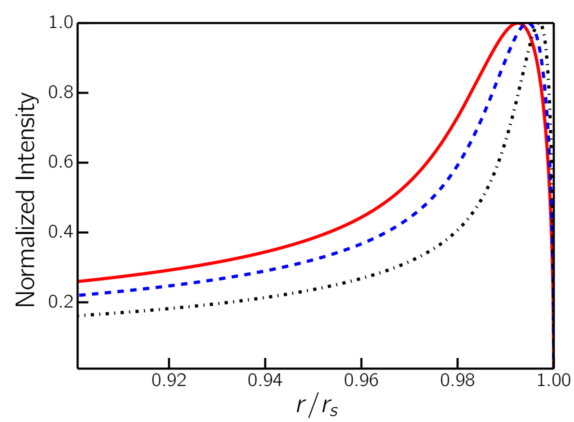

Fig. 2.— Calculated profiles in the loss-limited model for $B_0 = 100\mu G$, $\mu = 1/3$. The solid line represents a photon energy of 1 keV, the dashed line represents a photon energy of 2 keV, and the dot-dashed line represents a photon energy of 8 keV.

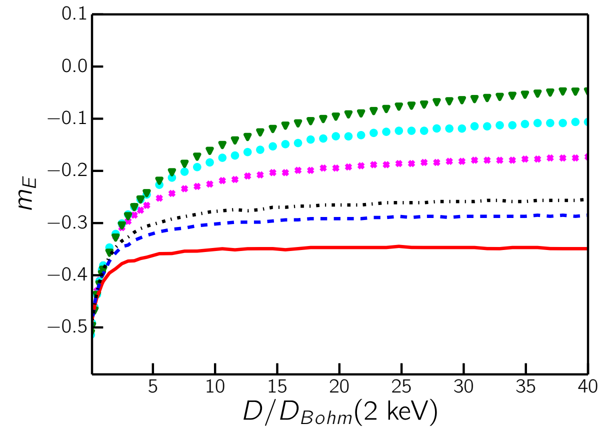

Fig. 3.— Dependence of the parameter $m_{\rm E}$ on the magnitude of the diffusion coefficient, D, measured in units of the Bohm value at a photon energy of 2 keV. Recall that $m_{\rm E}$ is defined such that the FWHM of the rim is $\propto E^{m_{\rm E}}$. The lines are, from bottom to top: $\mu = 0, 1/3, 1/2, 1$ (Bohm), 1.5, and 2. The calculations were done with $B_0 = 100\mu G$. For small values of D we find that all models converge to just below $m_{\rm E} = -0.5$, while for larger values of D clear limits can be placed on the range of $m_{\rm E}$, an observable quantity, for each value of μ (where $D \propto E^{\mu}$).

3.2. Magnetically Damped Model

In this model, we assume that the magnetic field amplification decays exponentially behind the shock, in the form of $B(x) = B_{min} + (B_0 + B_{min})\, e^{-x/a_b}$, with B_{min} taken to be $5\mu G$ (conservatively taken to be slightly higher with the above quoted value of 3 μG in the ISM). For this damped form of the magnetic field,

$$z(x) = \left(\frac{B_{min}}{B_0}\right)^2 x + 2a_b \frac{B_{min}(B_0 - B_{min})}{B_0^2}(1 - e^{-x/a_b}) + \frac{a_b}{2}\left(\frac{B_0 - B_{min}}{B_0}\right)^2 (1 - e^{-2x/a_b}). \quad (24)$$

In order to both produce the observed filament profiles and to be distinguishable from the loss-limited model, B_0 must be roughly at least four times B_{min}. There are three free parameters, η, B_0, and a_b, so with only two observational constraints the fits are not unique.

3.2.1. Energy Dependence in the Magnetically Damped Model

Again, neglecting the energy cut-off for a moment, we see key features develop in the energy dependence of the FWHM. At low photon energies, where losses are negligible over the small region a_b, rim sizes are energy-independent. Radial profiles at these energies reflect the spatial dependence of the magnetic field, and so, if this model is correct, we would expect thin filaments to be observed in high resolution radio images. At higher energies, the maximum value that m_E reaches is determined by the competition between a_b, $l_{\rm diff}$, and $l_{\rm ad}$. This can be roughly expressed by the equation

$$l_{\rm eff} = min\left[max\left(l_{\rm ad}, l_{\rm diff}\right), a_b\right]. \qquad (25)$$

Thus there are three possibilities. If $l_{\rm diff}$ is small enough, then as energy increases, synchrotron losses will "catch up" to a_b and there will be a clear transition between loss-limited rims and magnetically limited rims. If $l_{\rm diff}$ is large enough, the rims will be damping limited at all photon energies. Finally, if a_b is large enough, the rims will be loss-limited at all photon energies. It is worth noting that low-energy (i.e., radio) thin synchrotron filaments would be a clear signature of field damping. Examples of how the calculated profiles can vary with energy in 'strong' and 'weak' damping are plotted in Figure 4.

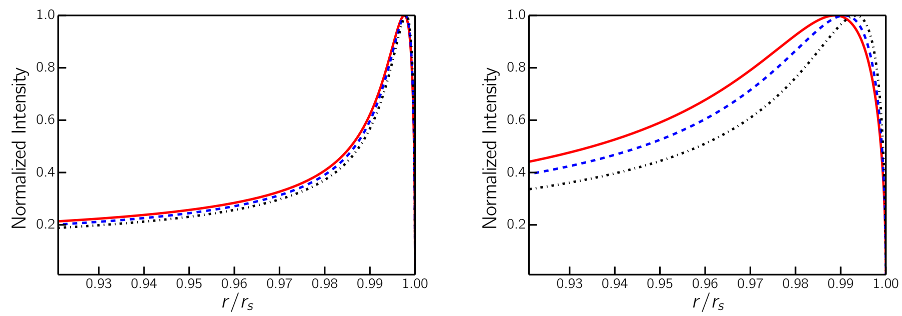

Fig. 4.— Calculated profiles in the magnetically damped model for $B_0 = 70\mu G$, $a_b = .005r_s$ (left) and $a_b = .05r_s$ (right). The solid line represents a photon energy of 1 keV, the dashed line represents a photon energy of 2 keV, and the dot-dashed line represents a photon energy of 8 keV.

3.3. Electron Cut-Off Energy and the Energy Dependence of Rim Widths

The fact that the injected spectrum of electrons has a cut-off above some energy $E_{\rm cut}$ has an impact on the energy dependence of the FWHMs of the observed intensity profiles. This is most easily seen in the δ-function approximation to the synchrotron emissivity for the case of a constant magnetic field B_0 in the absence of a cut-off in the electron distribution. Here $z(x)$ is just x, $E = \sqrt{\nu/(c_m B_0)} \equiv E_{\nu,0}$ and, using

$$f(E) = K(E_0(E))^{-s}\frac{dE_0}{dE} \tag{26}$$

and

$$E_0 = \frac{E}{1 - EbB_0^2t} = \frac{Ev}{v - EbB_0^2x} \equiv \frac{E_{\nu,0}}{1 - x/l_{\rm ad}} \tag{27}$$

from Reynolds (2009), we get for the spatial dependence of the emissivity (recalling that $j_\nu \propto \sqrt{\nu B} f(\nu, x)$ in this case)

$$j_\nu = C_j \left(1 - \frac{x}{l_{\rm ad}}\right)^{s-2} e^{\frac{-E_{\nu,0}}{E_{\rm cut}\left(1-\frac{x}{l_{\rm ad}}\right)}}. \tag{28}$$

When $E \gtrsim E_{\rm cut}$, the exponential term dominates the spatial behavior, resulting in an emissivity that will decay to half its peak at a distance $x_{1/2}$ given by

$$x_{1/2} = \frac{l_{\rm ad}}{1 + \frac{E_{\nu,0}}{E_{\rm cut}\ln(2)}}. \tag{29}$$

with an energy index of

$$m_E = \frac{\partial \log(x_{1/2})}{\partial \log(\nu)} = -\frac{1}{2}\left(1 + \frac{\nu^{1/2}}{E_{\rm cut}\sqrt{c_m B_0} + \nu^{1/2}}\right) = -\frac{1}{2}\left(1 + \frac{E_\gamma^{1/2}}{E_{\rm rolloff}^{1/2} + E_\gamma^{1/2}}\right) \tag{30}$$

So near the rolloff photon energy $E_{\rm rolloff} \equiv h\nu_{\rm m}(E_{\rm cut})$, $|m_E|$ is higher that the value of $1/2$ expected from pure advection. In the full numerical calculation, this arises as a shift in the expected m_E by some negative constant above some energy, even when diffusion is the dominant method of transport (see Figure 5).

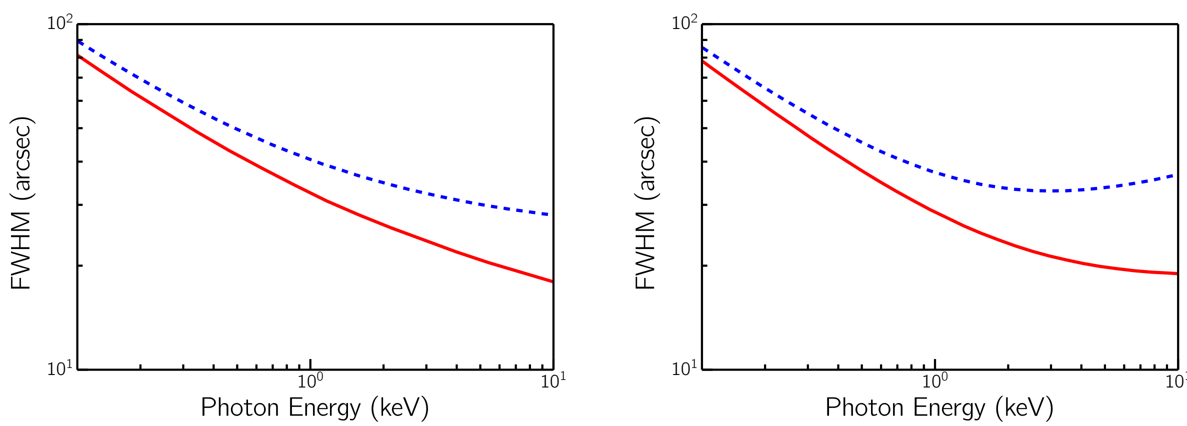

Fig. 5.— Demonstration of the effect of including a cut-off in the injected electron spectrum on the energy dependence of the filament widths for $\eta_2 = 2.6$, $B_0 = 100\mu G$, and for $\mu = 1$(left) and $\mu = 2$(right). Solid lines represent calculations with a cut-off in the electron spectrum and dashed lines represent calculations without a cut-off in the electron spectrum.

3.4. Shifts in Intensity Peak Location

In Figures 2 and 4 we see that in the presence of filament widths that shrink with energy there is an associated outward motion of the location of peak emission. Regardless of the underlying mechanism responsible for reducing the widths, that same mechanism explains this peak shift as it focuses the emission to increasingly narrow regions at higher energies. Thus this effect is a model-independent prediction.

However, determining the location of the peak emission from observations is a task much more uncertain than determining the FWHM of radial profiles. Furthermore, the predicted shift in location can be quite small ($\lesssim 1'$) for the best-fit parameters found in section 4. The combination of these two limitations leads us to ignore this effect in the rest of our analysis.

3.5. Comparison to the δ-Function Approximation

We first considered using the delta function approximation of the emissivity, namely

$$j_\nu \propto \sqrt{B\nu} f\left(x, E = \sqrt{\frac{\nu}{c_m B}}\right). \tag{31}$$

However, when compared with the full convolution of the particle distribution with the single electron emissivity, the results for the FWHMs disagree considerably (see Figure 6). What is worse, the difference is dependent on the electron energy so that a simple constant correction factor could not be employed. The combination of the δ-function approximation with the catastrophic dump form of the convection-diffusion equation seems to provide a much better approximation, but it does not account for the cut-off in the injected spectrum of electrons. Thus, we were compelled to use the full synchrotron emissivity in our numerical calculations coupled with the integral solution to the continuous energy loss convection-diffusion equation.

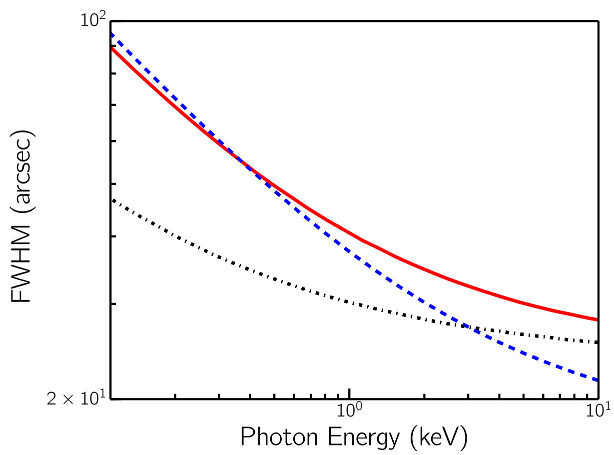

Fig. 6.— Comparison of the energy dependence of the FHWM for Bohm diffusion at $B_0 = 100\mu G$ and η=2.6 in different possible approximations without an electron cut-off. Similar differences were seen for other input parameters. Solid line represents a full convolution without a cut-off in the electron spectrum, dashed line represents the δ-function approximation used with the catastrophic dump convection-diffusion equation, and dot-dashed line represents the δ-function approximation used with the continuous energy loss convection-diffusion equation.

4. Results

In this section we first summarize our observational methodology in measuring the filament widths and spectra. Then we detail our fitting procedure for applying our model to the data and describe our findings.

To extract radial profiles of the NE and SW limbs of SN 1006, we use six *Chandra* observations, the parameters of which are summarized in Table 3. The observations of the SW and some of the NE were performed as part of a *Chandra* Large Program (Winkler et al. 2014). These new observations provide the first high quality image of the SW quadrant, comparable in quality with previous images of the NE. We reprocessed the level-1 event files with CIAO ver. 4.4 and CALDB ver.4.5.1. After correcting for vignetting effects and exposure times for all of the data sets, we extract radial profiles in three energy bands: 0.7–1 keV, 1–2 keV, and 2–7 keV from 22 regions shown in Figure 7. Each profile is binned by 1″. When combining the NE profiles from different epochs, we take into account the expansion of the remnant by 4" according to the literature (Katsuda et al. 2009; Winkler et al. 2014). Region 8 was excluded from this analysis because in the lowest energy bin there was spatial overlap between two filaments.

4.1. Profile Modeling

To estimate rim widths, we fit each profile with an empirical model defined as,

$$h(x) = \begin{cases} A_u \exp\left(\frac{x_0 - x}{w_u}\right) + C_u & \text{(upstream)} \\ A_d \exp\left(\frac{x - x_0}{w_d}\right) + B \exp\left(\frac{-(x-x_1)^2}{2\pi\sigma^2}\right) + C_d & \text{(downstream)} \end{cases} \tag{32}$$

where A_u, x_0, w_u, C_u, A_d, w_d, B, x_1, σ, and C_d are all free parameters. We note that either x_0 or x_1 can correspond to the peak of the X-ray profile, and that C_u represents the background level. The best-fit models are plotted as solid lines in Figures 8 and 9. Based on the best-fit model, we calculate a full width at half maximum (FWHM) for each profile. The model accounts for plateaus of emission upstream and downstream of the peak; the Gaussian component describes possible downstream features due to

Table 3. *Chandra* observations of SN 1006

ObsID	Array	R.A. (J2000)	Decl. (J2000)	Roll	Obs. Date	Exposure (ks)	PI
732	ACIS-S	15:03:51.7	-41:51:16	280.2°	2000 Jul 10	55.3	K.S. Long
9107	ACIS-S	15:03:51.5	-41:51:19	280.4°	2008 Jun 24	68.9	R. Petre
13738	ACIS-I	15:01:43.7	-41:57:55	25.3°	2012 Apr 23	73.5	P.F. Winkler
13739	ACIS-I	15:02:14.9	-42:06:49	9.1°	2012 May 4	100.1	P.F. Winkler
13743	ACIS-I	15:03:01.8	-41:43:05	19.9°	2012 Apr 25	92.6	P.F. Winkler
14424	ACIS-I	15:01:43.7	-41:57:55	253.1°	2012 Apr 27	25.4	P.F. Winkler

projection effects. Since our primary interest is in the energy-dependence of widths, the most important consideration is the consistency of a filament model among the three energy bins. To estimate the uncertainties of FWHMs, the best-fit profiles are artificially re-scaled (stretched or shrunk) along the x-axis, so that a new x-position of the model profile (x') becomes $x\left(1+\xi\times\frac{x-x_0}{200''-x_0}\right)$, where x is the original x-position of the model profile and ξ is a variable stretch factor. For various ξ-values, χ^2 values between the re-scaled model profile and the data are calculated, resulting in statistical uncertainties on a (and FWHM).

The best-fit FWHMs and their statistical uncertainties (ranges corresponding to $\Delta\chi^2 = 2.7$) are listed in Tables 4, 5, and 6. The results are categorized into four groups that appear to be along the same filaments. Also listed in Tables 4, 5, and 6 is the average value of $m_E \equiv \log(\mathrm{FWHM}/\mathrm{FWHM}')/\log(\nu/\nu') =$ either $\log(\mathrm{FWHM}/\mathrm{FWHM}')/\log(2/1)$ or $\log(\mathrm{FWHM}/\mathrm{FWHM}')/\log(1/0.7)$ for our purposes, taking the FWHM for each energy range as that of the lower limit and using the lower adjacent energy bin for the primed variables. This quantity characterizes the energy dependence of the FWHMs by writing them as $\propto E^{\mathrm{m_E}}$. To get the uncertainties on the calculation of m_{E} and the averages, we took the uncertainty on each data point as approximately symmetric with $\sigma = (\sigma_+ + \sigma_-)/2$.

To check the energy-dependence of rim widths, we extract two X-ray spectra from each region: one is taken from a filament region (covering from a shock front to a FWHM position downstream) and the other is taken from a plateau region next to the filament region up to a 2×FWHM position downstream. These spectra together with the best-fit models (`srcut` in XSPEC: Reynolds 1998) are presented in Figures 8 and 9, where black and red are responsible for the filament and the plateau regions, respectively. In some regions (e.g., region #3), spectral softening downstream is clearly seen. This is consistent with the fact that the higher the energy band, the narrower the rim widths become.

Table 4. Measured Filament FWHM (arcseconds) vs. Energy Band - Northeast Limb

Filament 1				Filament 2			
Region	0.7-1 keV	1-2 keV	2-7 keV	Region	0.7-1 keV	1-2 keV	2-7 keV
1	$36^{+2.3}_{-2.1}$	$33.4^{+1.5}_{-1.0}$	$33.3^{+2.3}_{-2.8}$	5	$25.8^{+.9}_{-1}$	$19.5^{+0.3}_{-0.6}$	$17.5^{+0.7}_{-0.7}$
2	$9.4^{+0.8}_{-0.7}$	$6.0^{+0.2}_{-0.3}$	$4.9^{+0.5}_{-0.3}$	7	$13.8^{+0.4}_{-0.3}$	$9.7^{+0.1}_{-0.2}$	$10.2^{+0.1}_{-0}$
3	$10.3^{+0.6}_{-0.6}$	$10.1^{+0.4}_{-0.4}$	$6.5^{+0.3}_{-0.2}$	9	$26.9^{+0.3}_{-0.6}$	$16.2^{+0.1}_{-0}$	$11.1^{+0.1}_{-0.1}$
4	$78.1^{+7.3}_{-6.8}$	$76.7^{+4.6}_{-4.6}$	$48.4^{+2.4}_{-2.2}$	10	$33.4^{+1.5}_{-1.3}$	$30.7^{+0.5}_{-0.5}$	$26.8^{+0.7}_{-0.6}$
6	$43.7^{+5.5}_{-3.3}$	$33.5^{+0.8}_{-0.9}$	$33.6^{+1.6}_{-1.6}$	11	$15.2^{+0.3}_{-0.2}$	$11.2^{+0.1}_{0}$	$10.9^{+0.9}_{-0.7}$
Average	36 ± 1.7	32 ± 1.0	25 ± 1.7	Average	23.0 ± 0.4	17.5 ± 0.14	15.3 ± 0.6
Average m_E		-0.30 $\pm$ 0.16	-0.3 $\pm$ 0.11	Average m_E		-0.78 $\pm$ 0.05	-0.19 $\pm$ 0.05

*When calculating the uncertainties on the average FWHM and the average m_E, the uncertainties on each individual FWHM were treated as symmetric with uncertainty $(\sigma_+ + \sigma_-)/2$. The average $m_{\rm E}$ is defined as the $m_{\rm E}$ calculated from the average FWHMs.

Table 5. Measured Filament FWHM (arcseconds) vs. Energy Band - Southwest Limb

Filament 3				Filament 4			
Region	0.7-1 keV	1-2 keV	2-7 keV	Region	0.7-1 keV	1-2 keV	2-7 keV
12	$12.4^{+1.7}_{-1.6}$	$14.2^{+1.0}_{-1.0}$	$11.0^{+0.9}_{-0.9}$	17	$35.2^{+2.8}_{-3}$	$27.1^{+1.2}_{-1.1}$	$20.5^{+1.6}_{-1.5}$
13	$50.8^{+2.6}_{-1.9}$	$54.9^{+2.3}_{-1.7}$	$38.0^{+2.9}_{-0.8}$	18	$24.2^{+1.5}_{-2.0}$	$29.9^{+0.9}_{-0.9}$	$19.0^{+1.2}_{-1.1}$
14	$38.6^{+2.2}_{-1.9}$	$33.6^{+1.3}_{-1.1}$	$27.7^{+3.2}_{-0.6}$	19	$13.7^{+1.1}_{-1.1}$	$15.1^{+0.6}_{-0.6}$	$6.9^{+0.6}_{-0.5}$
15	$69.9^{+3.8}_{-4.5}$	$47.5^{+1.1}_{-1.9}$	$23.7^{+1.5}_{-1.0}$	20	$34.2^{+3.0}_{-2.9}$	$39.8^{+1.5}_{-1.6}$	$27.0^{+0.1.6}_{-1.3}$
16	$74.0^{+5.2}_{-5.1}$	$63.6^{+2.1}_{-2.0}$	$46.3^{+2.3}_{-2.3}$	21	$35.0^{+1.7}_{-2.1}$	$14.0^{+0.9}_{-0.1}$	$12.3^{+0.1}_{-0.5}$
				22	$31.7^{+2.2}_{-1.9}$	$17.5^{+0.5}_{-0.8}$	$13.9^{+0.9}_{-1.2}$
Average	49 ± 1.5	42.8 ± 0.7	29.3 ± 0.8	Average	29.0 ± 0.9	23.9 ± 0.4	16.6 ± 0.5
Average m_E		-0.4 $\pm$ 0.10	-0.54 $\pm$ 0.04	Average m_E		-0.5 $\pm$ 0.10	-0.53 $\pm$ 0.05

*See note on Table 4

Table 6. Measured Filament FWHM (arcseconds) vs. Energy Band - Southwest Limb

Filament 5			
Region	0.7-1 keV	1-2 keV	2-7 keV
8	$23.8^{+2.0}_{-1.5}$	$20.9^{+1.0}_{-0.8}$	$15.9^{+0.8}_{-0.9}$
10	$33.4^{+2.5}_{-1.3}$	$30.7^{+5}_{-0.5}$	$26.8^{+0.7}_{-0.6}$
Average	24 ± 2	27.2 ± 0.6	24.8 ± 0.6
Average m_E		-0.6 $\pm$ 0.2	-0.14 $\pm$ 0.05

*See note on Table 4

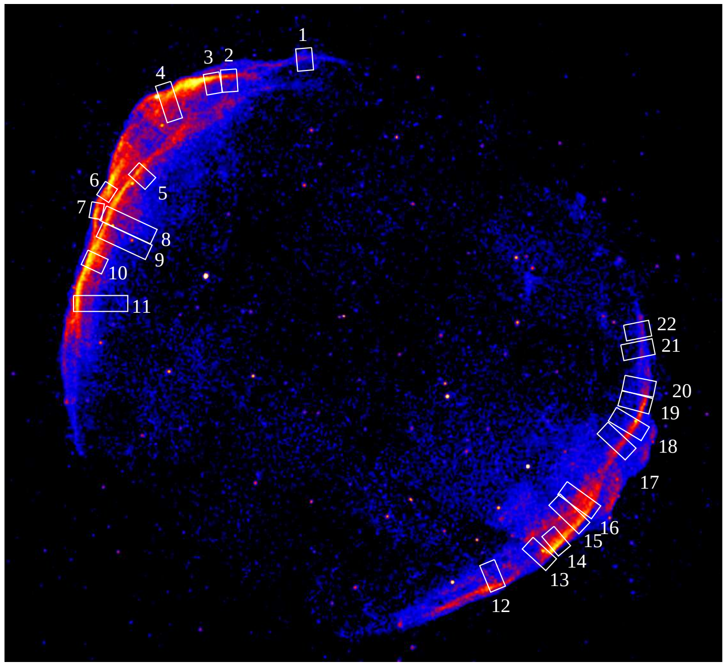

Fig. 7.— *Chandra* image at 2-7 keV showing the regions where radial profiles were extracted. Filament 1:Regions 1-4 and 6; Filament 2: Regions 5, 7, and 9-11; Filament 3: Regions 12-16; Filament 4: Regions 17-22; Filament 5: Regions 6 and 8

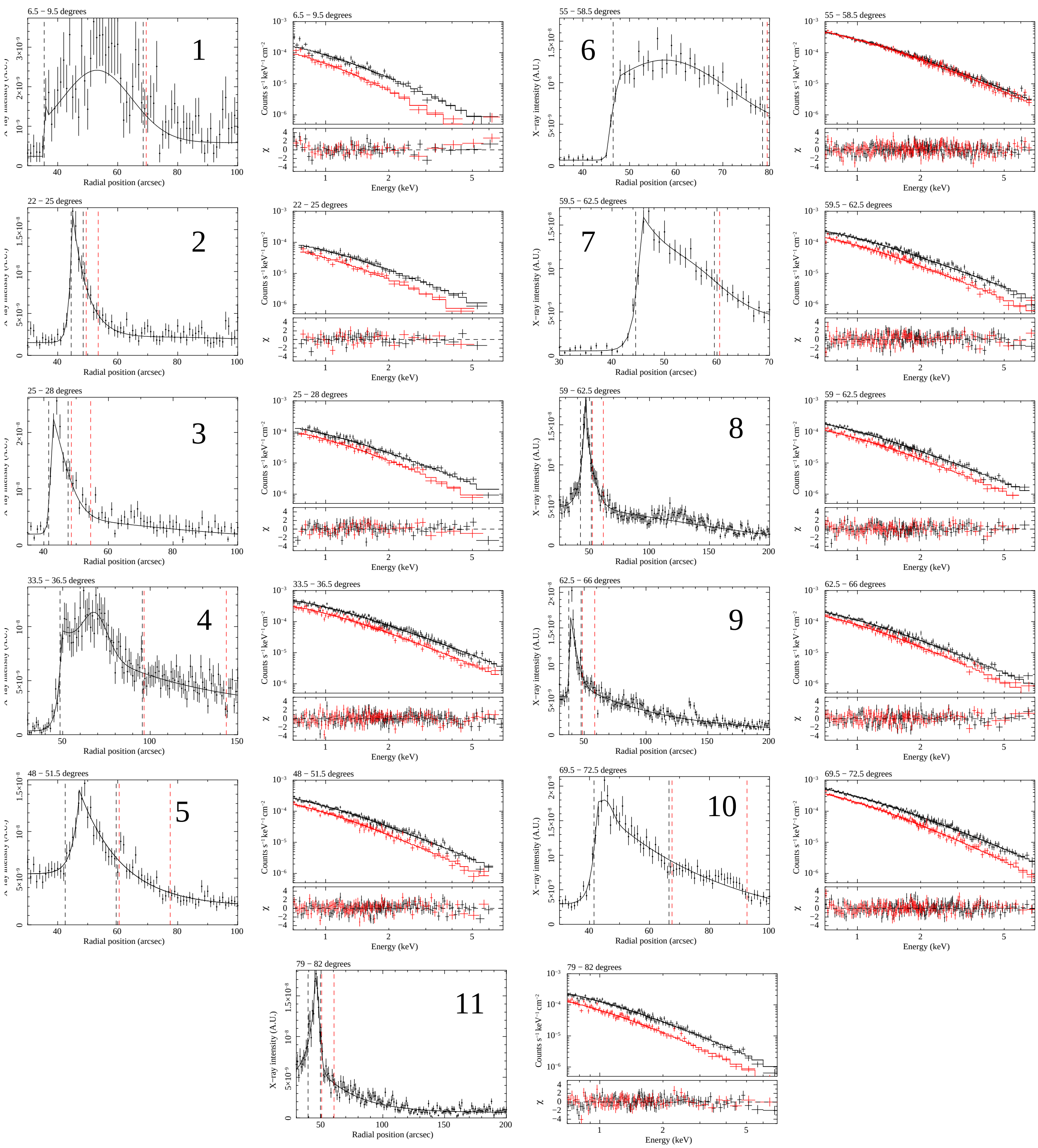

Fig. 8.— Left: Filament radial intensity profiles at 2-7 keV. The dashed, black vertical lines occur at a length of one FWHM on each side of the emission's peak, while the dashed, red vertical lines enclose the region extending towards the center of the remnant that starts at the edge of the black region to a distance of 2×FWHM away from the peak. Right: Energy spectra of the filaments separated into the same two regions

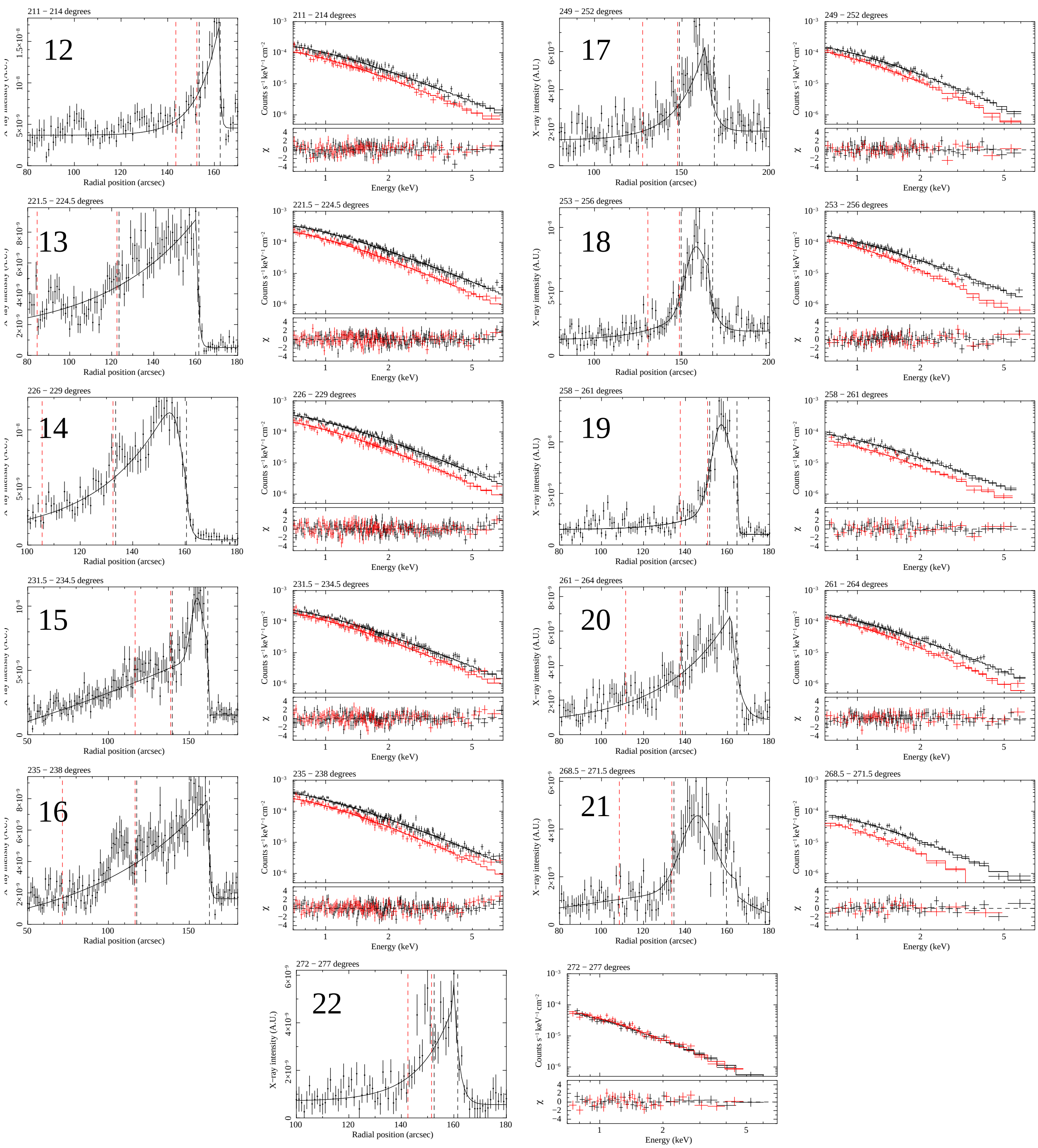

Fig. 9.— See Figure 8 caption

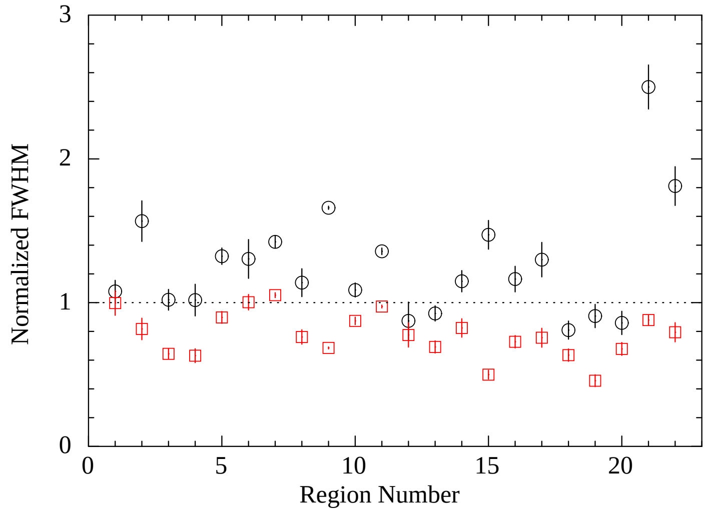

Fig. 10.— Observed energy dependence of the FHWMs of SN1006, plotted vs. region number and normalized to the middle (1–2 keV) energy band. Circles represent 0.7–1 keV while squares represent 2–7 keV

4.2. Fitting procedure

For each choice of spectral index for the power law dependence of the diffusion coefficient, μ, we constructed a two dimensional grid in the parameter space of $(B_0, \eta E_h^{1-\mu})$ for which we calculated radial profiles at 0.7, 1, and 2 keV for each point in the grid (recall that $\eta E_h^{1-\mu}$ is the constant scaling factor of the diffusion coefficient, D). From this, we obtained both the FWHM at 2 keV and the specific value of m_E at 2 keV from log(FWHM(2keV)/FWHM(1keV))/log(2). Thus we had numerical results for a large number of discrete points over this parameter space and manually found the point that simultaneously reproduced the values of both B_0 and η obtained from our observations.

We obtained the stated uncertainties by varying the parameters η and B_0 around this best-fit value to find the domain in which the observations were still satisfied within their respective uncertainties. While not a formal error-analysis, this procedure is adequate to put approximate lower and upper bounds on our estimates.

4.3. Loss-Limited Model

The best-fit parameters are shown in Table 7, where η_2 is the strength of the diffusion coefficient divided by the Bohm diffusion coefficient at an energy of $\sqrt{\nu/c_m B_0}$, which depends also on the fitted value for B_0. Note that this calculation included the convolution of the single particle emissivity with the solution of the continuous energy loss convection-diffusion equation for a spectrum of electrons exponentially cut off at the shock.

.

4.4. Magnetically Damped Model

The magnetically damped model predicts that the data should show FHWMs that are only weakly dependent on energy, caused by the electron distribution's cut-off, with values of $m_{\rm E}$ on the order of -0.1. This is decidedly not what we observe, as the averaged filaments all display values of $|m_{\rm E}| \gtrsim 0.14$ at 2 keV and $\gtrsim 0.3$ at 1 keV. This does not demonstrate that post-shock magnetic field damping cannot occur, or that rims might not be magnetically damped at much lower observation energies, but it provides sufficient evidence that the damping length must at least be large enough to be unimportant, i.e., larger than the synchrotron-loss length, for electrons radiating at keV energies. Therefore, we confidently conclude that the X-ray rims of SN1006 are *not* well described by the magnetically damped model.

Table 7. Best fit parameters for the Filaments in varying values of μ (Numerical Results)

	Filament 1		Filament 2		Filament 3	
μ	η_2	B_0	η_2	B_0	η_2	B_0
0	7.5 ± 2	142 ± 5	-	-	$\lesssim 0.1$	77 ± .8
1/3	4 ± 1.3	120 ± 5	-	-	$\lesssim 0.1$	76 ± 1.4
1/2	3 ± 1.1	112 ± 4	-	-	$\lesssim 0.1$	75 ± 1.0
1	2 ± 1.0	100 ± 3	22 ± 3	214 ± 4	$\lesssim 0.1$	74 ± 1.1
1.5	1.9 ± 1.2	95 ± 3	9 ± 1.2	167 ± 4	$\lesssim 0.1$	74 ± 1.2
2	2 ± 1.0	92 ± 4	7 ± 1.1	152 ± 4	$\lesssim 0.1$	73 ± 1.2

	Filament 4		Filament 5	
μ	η_2	B_0	η_2	B_0
0	$\lesssim 0.2$	113 ± 2	-	-
1/3	$\lesssim 0.2$	112 ±2	-	-
1/2	$\lesssim 0.2$	111 ±2	-	-
1	$\lesssim 0.2$	109 ± 2	$80\,^{+\infty}_{-4}$	206 ± 3
1.5	$\lesssim 0.2$	108 ± 2	19 ± 2	140 ± 2
2	$\lesssim 0.2$	107 ± 2	12 ± 1.0	120 ± 2

*Results of fitting the data using our generalized diffusion model for the loss-limited case outlined in Section 3. Dashes denote places where fits were unobtainable. See note on Table 2 for B_0 and η_2

5. Discussion

In this section we will analyze the results of applying our model of Section 3 to the SN1006 data presented in section 4.

In fitting the data for various values of μ, we were able to acquire the best fit diffusion coefficient energy relation in the region in which electron energies are relevant for keV emission.

Fitting the data allowed us to constrain both the magnitude and the energy-dependence of the diffusion coefficient D, where the latter is reflected in the values of μ for which we could obtain fits. However, fixing the magnitude of D at some energy only fixes the combination $\eta E_h^{1-\mu}$, so there is a degeneracy in the choice of η and E_h. There are two restricting conditions. The first is that $D(E) > D_B(E)$ at all energies, as the Bohm coefficient is the minimum allowable. In other words,

$$\eta \left(\frac{E}{E_h}\right)^{\mu-1} > 1. \tag{33}$$

For $\mu > 1$, this restricts E^{μ} diffusion to above some threshold energy E_h, while for $\mu < 1$, this restricts E^{μ} diffusion to below some maximum energy E_h. It also means that the constant η must always be greater than 1 as $D(E_h)/D_b(E_h) = \eta$. The second restriction is that E_h should be outside the relevant energy range for electrons emitting keV X-rays, as all of our calculations had a fixed value for μ. What we can find, however, is the minimum (for $\mu < 1$) or maximum (for $\mu > 1$) value of this energy bound by fixing η at 1. For our successful fits that have non-negligible diffusion coefficients, the results of doing this give values of E_h that are so far outside the 0.7–7 keV photon range that we can easily find an appropriate E_h to satisfy the above conditions.

From Tables 2 and 7, we see that several of our averaged filaments require very small diffusion coefficients, well below the Bohm value, even using the amplified magnetic field.

This obviously implies that varying the parameter μ will have no effect on the fits, as is evident in the fitted values for B_0. Qualitatively, this means that the transport of electrons is being carried out dominantly by the convection of plasma away from the shock, and that each electron will stay attached to its particular fluid element. This result is required by the strong energy dependence ($m_{\rm E} \sim -0.5$) of the filament widths, as the presence of diffusion will always drive $m_{\rm E}$ towards 0 (or beyond to positive numbers in the case of $\mu > 1$. On the other hand, filaments with non-negligible diffusion coefficients are all consistent with the condition that $D > D_{\rm Bohm}$, within their respective uncertainties. This may suggest that some mechanism is severely limiting electron diffusion in various regions of the remnant, primarily the SW.

One shortcoming of the magnetically damped model is the requirement that $B(x)^2 D$ is constant. This implies that the diffusion coefficient varies as $1/B(x)^2$, when we have explicitly written the diffusion coefficient as proportional to $1/B(x)$ in our formalism. However, this does not affect our conclusion that the magnetically limited model is a poor fit to the data, as the qualitative behavior of the FWHMs as a function of energy would be the same. This requirement presents no issues in the case of the loss-limited model, as both D and B are spatially uniform in the narrow region behind the shock.

Our finding that rim widths drop too rapidly with energy to allow significant diffusion suggests the possibility of "sub-Bohm diffusion" ($\lambda < r_g$, or $\eta < 1$) in astrophysical sources. This possibility has important implications for acceleration times, since much smaller diffusion coefficients D would result in much shorter acceleration times to a given energy. There has been considerable discussion of the possibility of sub-Bohm diffusion in the literature. For instance, Zank et al. (2006) find that in perpendicular shocks in the solar wind, effective mean free paths can be an order of magnitude or more less than the gyroradius. They find some supporting evidence in heliospheric observations.

Using a 3D hybrid MHD-kinetic code, Reville & Bell (2013) studied the development of shock precursors generated by accelerated particles, finding sub-Bohm behavior for both parallel and oblique shocks, but more pronounced for parallel shocks. However, some of their simulations find that the Bohm limit is still respected using the amplified magnetic field. Reville & Bell discuss other possible ambiguities in the definition of the Bohm limit, including the possibility of highly inhomogeneous magnetic fields on small scales. At any rate, it seems clear that the complexities of the propagation of particles in the presence of dynamic self-generated magnetic turbulence are such that the suppression of diffusion to levels considerably below those implied by the Bohm limit is not ruled out by theoretical considerations. We emphasize that in spite of the elaborate theoretical structure we have presented, our limits on the diffusion coefficient are closely related to the rapid drop in filament widths with photon energy that we see. The rate of shrinkage is too large to tolerate much particle diffusion, independently of detailed modeling. However, detailed quantitative statements are dependent on the details of our mechanism for fitting filament widths, and on inevitable projection and curvature effects. Our models do predict considerably thinner filaments at 4 keV than at 2; while our current observations do not have adequate photon statistics to test this prediction, future studies should be performed to clarify this important issue.

Finally, we call attention to the μ dependence in the electron cut-off energy used in our model as described in Equation (19). For a synchrotron emitting source, this cut-off energy corresponds to a rolloff frequency of $\nu_{roll} \propto E_{cut}^2 B_0 \propto B_0^{(\mu-1)/(\mu+1)} v_s^{4/(\mu+1)}$. If $\mu = 1$ as in the standard Bohm assumption, we find a rolloff frequency that is independent of the magnetic field and solely a function of the shock speed. In that case, we would expect constant rolloff frequencies along the same filaments and only a relatively weak azimuthal dependence, predictable from observed proper motions. On the other hand, if $\mu \neq 1$, then we recover a B_0 dependence, which could account for the some of the systematic order-of-magnitude azimuthal variation of the measured rolloff frequencies seen in both SN1006 (Katsuda et al. 2010, Miceli et al. 2009, Reynolds et al. 2012) and G1.9+0.3 (Reynolds et al. 2009). For $\mu = 2$, one would require a very large variation in B_0, largest at the brightness maxima, to explain the observed factor of 10 range in rolloff frequency, however.

5.1. Comparisons to Cas A

A detailed application of our results to other SNRs such as Cas A will require much more extensive analysis, but we can use the published filament widths of Araya et al. (2010) for Cas A to get preliminary estimates of the magnetic field strength and diffusion coefficient by applying our model. In their data, it appears that the filaments in Cas A shrink by a factor of ~ 0.8 between 0.3 and 3 keV, while the filament widths appear to be energy-independent between 3 and 6 keV. Qualitatively, this is consistent with the loss-limited model, as our parameter $m_{\rm E}$ is predicted to decrease with energy. For the lower energy range of 0.3–3 keV, reproducing $m_{\rm E} \sim -0.1$ (equivalent to the factor of 0.8 drop in size) requires magnetic fields on the order of 200-500 μG and diffusion coefficients about $5 \times D_{\rm Bohm}(3 \text{ keV})$, about an order of magnitude higher than the values one obtains by neglecting the energy dependence. One can also see directly from Figure 3 that $\mu < 1$ models of the diffusion coefficient are excluded for $m_{\rm E} \sim -0.1$.

6. Summary and Conclusions

We have outlined a generalized diffusion model that solves the continuous energy-loss convection-diffusion equation for electrons subject to both convection and diffusion as they travel away from the shock. This model is able to incorporate arbitrary power-law energy dependence of the diffusion coefficient D, in the form of $D \propto E^{\mu}$, as well as arbitrary spatial dependence of the magnetic field strength. Assuming spherical symmetry, we then convolved this electron distribution with the single electron power spectrum to obtain a non-thermal emissivity, which we integrated along lines of sight to obtain the specific intensity of the source as a function of radial distance from its center. We specialized this model into two general categories: a "Magnetically Damped Model," which assumes $B \propto \exp^{-x/a_b}$ for x defined as the distance behind the shock, and a "Loss-limited Model" which assumes a constant post-shock magnetic field strength. Furthermore, we selected specific values of the parameter μ (namely 0,1/3, 1/2, 1, 1.5, and 2) to analyze. We found that independent of model details, magnetically damped models predict rim widths almost independent of photon energy, while loss-limited models predict rim widths to shrink with increasing photon energy at a rate dependent on the diffusion coefficient. Our quantitative results are summarized in Figure 3.

With this model as our guide, we used *Chandra* observations of SN 1006 to measure the energy dependence of the thin, non-thermal rims in the NE and SW quadrants. For the SW, these are the first such measurements, utilizing data from a recent Large *Chandra* Project. The SW filament profiles are of similar width to those in the NE. This is consistent with the results of Winkler et al. (2014), who find the conditions in both regions to be similar. Furthermore, the filament widths of SN1006 show a decrease with photon energy, which we have shown has important physical consequences for both the diffusion coefficient and the post-shock magnetic field, and is incompatible with a magnetic damping model. In the other SNRs for which magnetic fields have been inferred from rim thicknesses, the energy dependence of the widths should be examined similarly, as evidenced by our quick comparison with the results of Araya et al. (2010) for Cas A.

Using our generalized diffusion model and its subsets outlined above, we find the measured widths of the SW filaments of SN 1006, like those previously reported for the

NE, favor magnetic fields on the order of 100 μG, significantly amplified above the typical interstellar medium value of about 3 μG. The strength of our model is that it encompasses all effects included by previous authors in this type of investigation.

We also conclude that for the filaments of SN 1006 , and even the filaments of Cas A, values of $\mu < 1$ are, for the most part, less able to reproduce the data. This is due to the result that the lowest possible $m_{\rm E}$ for a given diffusion coefficient is $(\mu - 1)/4$, which requires $\mu \gtrsim 1$ in Filaments 2 and 5 for SN 1006 and the majority of filaments in Cas A (Araya et al. 2010). While not conclusive, this result is in agreement with the calculations of Reynolds (2004), which predict SNR images that do not resemble observed SNRs for $\mu < 1$. Thus both Kolmogorov turbulence ($\mu = 1/3$) and Kraichnan ($\mu = 1/2$) are disfavored. In an application to other SNRs, values of $\mu > 1$ allow completely energy-independent filament widths even with a cut-off in the injected spectrum of electrons. Thus, the results of Araya et al. (2010), who found energy independent FWHMs in Cas A between 3-6 keV, could result from strong diffusion and a very high electron cut-off energy, or from non-Bohm-like diffusion with $\mu > 1$. In the latter case, our model also predicts that the rolloff frequency should depend on magnetic field strength and thus could have significant azimuthal dependence.

We also find that that the magnitudes of the diffusion coefficients in the filaments of SN1006 are split into two distinct categories. One group, due to the strong energy dependence of their filament widths, requires negligible amounts of diffusion (i.e. less than the Bohm limit) in order to reproduce the observations. The occurrence of sub-Bohm diffusion is thus far undocumented and would be a groundbreaking result. However, there are inherent uncertainties in our measurements of the FWHMs due to projection, overlap, and averaging effects which may have influenced our numerical calculations. Thus, we do not claim strong evidence of this theoretically hard to explain phenomenon and note that further study is needed. On the other hand, we are much more confident in the rest of our conclusions, which are fairly robust and do not depend on sub-Bohm diffusion. The second group, with less energy-dependent filament widths, is consistent with diffusion coefficients close to but above the Bohm limit. This result is of interest because the strength of diffusion is directly tied to the maximum energy attainable by electrons being accelerated at the shock front. Diffusion coefficients much larger than the Bohm value would have suggested weaker scattering, which in turn would reduce the maximum energy (Reynolds 1998). However, in our model of the filaments, the radial profiles are produced by electrons in the post-shock region, so pre-shock electrons could have much different diffusive properties. Our fits predict continuing shrinkage of filament widths at higher energies than 2 keV, though photon statistics in our current observations are not adequate to test this. (Our 2–7 keV band is dominated by photons near 2 keV.) A longer observation of the SW region of SN 1006 with *Chandra* could allow division of that band into 2 – 4 and 4 – 7 keV bands, permitting this important test. Our surprising result of rapid shrinkage of some filaments requiring sub-Bohm diffusion coefficients can be searched for in other thin-rim remnants such as Tycho.

Finally, we find that the results of applying our generalized diffusion model are remarkably consistent with the results obtained by simply fitting Equation 6 to the data (recall that Equation 6 was the result of applying the δ-function approximation for the electron spectra to the catastrophic dump version of the convection-diffusion equation). This is in spite of the fact that our model solves the continuous energy loss convection-diffusion equation for the electron distribution, uses the full synchrotron emissivity, and includes a cutoff in the injected spectrum of electrons, all of which we have shown to have important effects on the FWHMs and their energy dependence. This may simply be a unique result for the observational data from SN1006, or it could suggest that the the effects of adding each of these more detailed considerations cancel each other out when combined. On the other hand, Equation 6 is incapable of describing magnetically damped filaments, which may occur in other remnants (e.g., Marcowith & Casse 2010), though we have ruled this out for SN1006.

The general formalism presented here is applicable to the thin, non-thermal filaments observed in nearly all historical SNRs, and has the potential to provide a consistent estimate of magnetic-field amplification across the variety of ambient environments into which these remnants are expanding.

Support for this work was provided by the National Aeronautics and Space Administration through *Chandra* Grant Number GO2-13066, issued by the *Chandra* X-ray Observatory Center, which is operated by the Smithsonian Astrophysical Observatory for and on behalf of NASA under contract NAS8-03060.

We thank the anonymous referee for an extremely careful reading of this paper, and for suggestions that have led to substantial improvements.

A. Appendix

We summarize here some details of the relation of our models to observations. Our basic conclusion is that the variation of filament widths with energy contains essential information required to compare models, and to obtain quantitative estimates of the magnetic field and diffusion coefficient. Without this information, there are several competing models that can allow for a wide range of magnetic-field strengths and diffusion coefficients for the same filament width.

We assume throughout a spherical shock surface, in which the peak of synchrotron emission occurs at a radius slightly behind the shock due to the geometry of the line of sight integration. If instead a plane shock with velocity exactly in the plane of the sky is assumed, derived quantities will vary somewhat. In addition, we find that the δ-function approximation gives a poor representation of the spatial distribution of high-energy electrons, resulting in an underestimate of filament widths. It is also essential to consider the cutoff in the electron spectrum above some maximum energy as it causes filament widths to shrink with photon energy in a model-independent way. At photon energies close to the rolloff frequency, the only way to have truly energy-independent rim sizes is with $\mu > 1$. In energy-loss models with $\mu \leq 1$, or damping models, $|m_{\rm E}|$ will always be at least ~ 0.1 if the cutoff is not exceptionally high (well above the keV band).

Then the strength of the energy-dependence of filament widths serves as the essential discriminant among models. If a weak energy dependence ($0.1 \lesssim |m_{\rm E}| \lesssim 0.2$) is observed for photon energies near the synchrotron rolloff frequency, the behavior at lower photon energies should be inspected as it will have greater discriminatory power. Here "lower energies" means energies lower than those where diffusion and the electron cutoff start to become important, which depend on the source parameters. Near the rolloff frequency, many effects can combine to cause weak energy-dependence of filament widths.

If moderately strong energy-dependence of filament widths is observed ($0.2 \lesssim |m_{\rm E}| \lesssim 0.5$) at a specific energy, then a magnetic-field damping model can be ruled out at that energy and above. This is the region in which it can be assumed that diffusion is important in competing with advection. The details of this then depend on the assumed model of diffusion. And if very strong energy-dependence of filament widths is observed ($|m_{\rm E}| \gtrsim .5$) then the only explanation is weak diffusion and the predominance of advection as the electron transport mechanism.

Finally, if filaments widths are ever observed to be growing with energy then the only known explanation would be $\mu > 1$ diffusion. Higher values of μ allow for more rapid changes in m_E as a function of energy.

REFERENCES

Abraham, J., et al. 2008, PRL, 101, 061101

Acero, F. et al. 2010, A&A 516, A62

Araya, M., Lomiashvili, D., Chang, C., Lyutikov, M. & Cui, W. 2010, ApJ, 714, 396

Ballet, J., 2006, Adv. Sp. Res., 37, 1902

Bamba, A., Yamazaki, R., Ueno, M., & Koyama, K. 2003, ApJ, 589, 827

Bamba, A., Yamazaki, & Hiraga, J. S., 2005, ApJ, 632, 294

Berezhko, E. G., & Völk, H. J., 2004, A&A, 419, L27

Berezhko, E. G., Ksenofontov, L. T., & Völk, H. J. 2003, A&A, 412, L11

Burbidge, G.R. 1956, ApJ, 124, 416

Cassam-Chenaï, G., Hughes, J. P., Ballet, J., & Decourchelle, A. 2007, ApJ, 665, 315

Green, D. A. 2009, Bulletin of the Astronomical Society of India, 37, 45

Jun, B.-I., & Jones, T.W. 1999, ApJ, 511, 774

Katsuda, S., Petre, R., Long, K. S., et al. 2009, ApJL, 692, 105

Katsuda, S., Petre, R., Mori, K., Reynolds, S.P., Long, K.S., Winkler, P.F., & Tsunemi, H. 2010, ApJ, 723, 383

Lagage, P.O., & Cesarsky, C.J. 1983, A&A, 125, 249

Lerche, I., & Schlickeiser, R. 1980, ApJ, 239, 1089

Lyne, A.G., & Smith, F.G. 1989, MNRAS, 237, 533

Lyutikov, M., & Pohl, M. 2004, ApJ, 609, 785

Marcowith, A., & Casse, F. 2010, A&A, 515, A90

Pacholczyk, A.G., 1970, *Radio Astrophysics* (San Francisco: Freeman).

Morlino, G., Amato, E., Blasi, P., & Caprioli, D. 2010, MNRAS, 405, L21

Miceli et al. 2009 A&A 501, 239

Parizot, E., Marcowith, A., Ballet, J., & Gallant, Y. A. 2006, A&A, 453, 387

Pohl, M., Yan, H., & Lazarian, A. 2005 ApJ, 626, L101

Reville, B., & Bell, A.R. 2013, MNRAS, 430, 2873

Reynolds, S. P. 1998, ApJ, 493, 375

Reynolds, S. P. 2004, Adv. Sp. Res., 33, 461

Reynolds, S. P. 2009, ApJ, 703, 662

Reynolds, S. P., Borkowski, K. J., Green, D. A., et al. 2009, ApJL, 695, L149

Reynolds, S.P., Gaensler, B.M., & Bocchino, F. 2012, Space Science Reviews, 166, 231

Rettig, R., & Pohl, M. 2012, A&A, 545, A47

Tanimori, T. et al. 1998, ApJL, 497, L25

Vink, J., & Laming, J. M. 2003, ApJ, 584, 758

Völk, H. J., Morfill, G.E. & Forman, M.A., 1981, ApJ, 249, 161

Winkler, P. F., Gupta, G., & Long, K. S. 2003, ApJ, 585, 324

Winkler, P.F., et al. 2014, ApJ, in press

Yamazaki, R., Yoshida, T., Terasawa, T., Bamba, A., & Koyama, K. 2004, A&A, 416, 595

Zank, G.P., Li, G., Florinski, V., Hu, Q., Lario, D., & Smith, C.W. 2006, JGR, 111, A06108

Table 8. Symbol Glossary (Numerical values in CGS)

Symbol	Expression/Value	Explanation
	Diffusion Coefficient, $\mathrm{D} = \eta D_{\mathrm{B}}(E_h)\left(\frac{E}{E_h}\right)^{\mu}$	
D_B	$\frac{C_{\mathrm{d}}E}{B}$	"Bohm-limit" of D
C_{d}	2.083×10^{19}	
η		Scaling factor of D
μ		Power index for D with E
E_h		Arbitrary energy (keeps η dimensionless)
η_2	$\frac{D}{D_{\mathrm{B}}}(2\ \mathrm{keV})$	Relative D at $h\nu$=2 keV
	Synchrotron Parameters	
τ_{synch}	$\frac{1}{bB^2E}$	Synchrotron lifetime
l_{ad}	$\frac{v_s}{4}\tau_{synch}$	Advective length
l_{diff}	$\sqrt{D\tau_{synch}}$	Diffusive length
ν_m	c_mE^2B	δ-function synchrotron frequency
c_m	1.82×10^{18}	
c_1	6.27×10^{18}	
b	1.57×10^{-3}	
	Diffusion Model Parameters	
B_0		Immediate Post-shock B-field
$x_{1/2}$		FWHM of radial intensity profile
m_{E}	$\frac{\partial \log(x_{1/2})}{\partial \log(E_\gamma)}$	Power index of $x_{1/2}$ with E_γ
f(x,E)		e^- spatial and energy distribution
a_b		Length scale in B-damping model

Table 8—Continued

Symbol	Expression/Value	Explanation
	SN1006 Parameters	
$v_s^{\rm a}$	5×10^8	Shock Velocity
$r_s^{\rm b}$	2.96×10^{19}	Shock Radius
s	2.2	e^- spectral index

[a]Katsuda et al. 2009

[b]Calculated using the angular size in Green's catalog (2009) and the distance to the remnant given by Winkler et al. (2003)